THE ASTROPHYSICAL JOURNAL, 448:119–137, 1995 July 20

LINE STRENGTH GRADIENTS IN ELLIPTICAL AND BRIGHTEST CLUSTER GALAXIES

DAVID FISHER,[1,2] MARIJN FRANX,[1,3] AND GARTH ILLINGWORTH[2]
fish@astro.rug.nl, franx@astro.rug.nl, and gdi@lick.ucsc.edu
Received 1994 October; accepted 1995 January 30

ABSTRACT

Line strengths and their gradients in Mg, Fe, and Hβ have been determined for seven elliptical and nine brightest cluster galaxies (BCGs) in order to study their stellar populations and investigate their relationship to one another. We find that BCGs follow the same relationship between central Mg *b* line strength and central velocity dispersion found for elliptical galaxies. Brightest cluster galaxies are in agreement with the known trend toward more massive elliptical galaxies having larger [Mg/Fe] ratios, while the internal gradients *within* our BCG and E galaxies are consistent with a roughly constant [Mg/Fe] ratio. We find that a correlation exists between the central [Mg/Fe] ratio and average Hβ line strength in the sense that both BCG and elliptical galaxies with larger [Mg/Fe] ratios have lower $\langle$H$\beta\rangle$ strengths. For our sample, Hβ is the best predictor of [Mg/Fe] ratio. If the dominant contribution to the Hβ feature is from turnoff stars then this relation predicts that more massive elliptical galaxies are older than less massive ones. If, however, the main source of the Hβ index is from horizontal-branch stars, then the observed {[Mg/Fe],Hβ} relation could be the result of more massive elliptical galaxies having flatter IMFs for high-mass stars than less massive elliptical galaxies.

The $\langle$H$\beta\rangle$ line strengths of the objects in our sample span a range of values. The BCGs generally have low global Hβ line strengths, which, under the assumption that the Hβ feature can be used as an age discriminant, indicates that the bulk of these systems underwent their last major episode of star formation $\gtrsim$8–10 Gyr ago. For both the elliptical galaxies and BCGs we find that *within* a galaxy, the Hβ profile is flat for objects whose Hβ absorption can be reliably measured. In the presence of a declining metallicity gradient this suggests that the centers of elliptical galaxies and BCGs are $\sim$1–3 Gyr younger than their outer regions. The metal line strength gradients for the elliptical galaxies and BCGs are similar and consistent with an average gradient of Δ[Fe/H]/Δ log $r = -0.25 \pm 0.1$, corresponding to a reduction in the mean metallicity of the stellar population by a factor of $\sim$2 over a factor of 10 in radius. No strong correlations are found between the metallicity gradient sizes and either kinematic or line strength parameters of the galaxies. For the galaxy NGC 4073, the brightest member of the poor cluster MKW 4, we find enhanced Hβ absorption in the region coincident with the counterrotating stellar core. These observations are consistent with a scenario in which the accreted object was a younger system and/or a recent episode of star formation was triggered by an interaction.

Subject headings: galaxies: abundances — galaxies: elliptical and lenticular, cD — galaxies: stellar content

1. INTRODUCTION

This paper is the second part of a program to measure the kinematic and chemical properties of brightest cluster galaxies (BCGs). The first part of the project was the determination of the stellar kinematics of 13 BCGs through absorption-line rotation curves and velocity dispersion profiles (Fisher, Illingworth, & Franx 1995, hereafter FIF). The work presented here consists of the study of the stellar populations of seven elliptical galaxies and nine BCGs by way of an analysis of their line strengths and gradients in Mg, Fe, and Hβ.

The study of absorption-line strengths and their gradients in early-type galaxies is useful for understanding the formation and evolutionary processes occurring in these systems. Beginning with the early pioneering efforts (e.g., Faber 1973, 1977), the number of line strength studies has grown steadily (Efstathiou & Gorgas 1985; Rose 1985; Couture & Hardy 1988, hereafter CH; Gorgas, Efstathiou, & Salamanca 1990, hereafter GES; Boroson & Thompson 1991; Delisle & Hardy 1992; Worthey, Faber, & González 1992, hereafter WFG; Davidge 1992; Davies, Sadler, & Peletier 1993, hereafter DSP; González 1993; Carollo, Danziger, & Buson 1993, hereafter, CDB; Bertola, Burstein, & Buson 1993; Carollo & Danziger 1994a, b). From these and other investigations, a number of results concerning line strength behavior have emerged:

1. Early-type galaxy Mg line strengths are well correlated with central velocity dispersion (Faber 1973; Terlevich et al. 1981; Dressler 1984; Dressler et al. 1987; Burstein et al. 1988; Bender, Burstein, & Faber 1993, hereafter BBF). From a large sample ($\gtrsim$100 cE, dE, luminous E, and S0 bulges) BBF found that central velocity dispersion is the best indicator of the metallicity of dynamically hot galaxies—a single mean relation between Mg_2 index and σ_0 holds over four orders of magnitude in mass and surface brightness.[4]

2. Nearly all galaxies show declining Mg and Fe line strengths with increasing radius, which is most often interpreted as a decline in the overall metallicity (taken to be [Fe/H]). Although age and metallicity changes are difficult to disentangle (see Worthey 1994 and references therein), a number of studies have derived metallicity gradients based on

[1] Kapteyn Astronomical Institute, University of Groningen, P. O. Box 800, 9700 AV Groningen, The Netherlands.
[2] UCO/Lick Observatories, Board of Studies in Astronomy and Astrophysics, University of California, Santa Cruz, CA 95064.
[3] Harvard-Smithsonian Center for Astrophysics, 60 Garden Street, Cambridge, MA. 02138.

[4] None of the nine BCGs in our study are in the BBF sample.

measured Mg and Fe gradients using theoretical and empirical calibrations. In this way, metallicity gradients of $\Delta \log [Fe/H]/\Delta \log r \approx -0.20$–$0.30$, or a reduction in mean metallicity of 40%–50% over a decade in radius, have been quoted—implying that metallicity gradients in elliptical galaxies are quite shallow (e.g., Thomsen & Baum 1989; GES, CH, DSP; González 1993).

3. The ratio of Mg to Fe is greater than the solar value in luminous elliptical galaxies (Peletier 1989; GES; WFG). The level of Mg enhancement is large, ~ 0.2–0.3 dex with respect to the most metal-rich stars in the solar neighborhood, and cannot be explained by simple scalings of solar abundances or realistic changes to the model ages (WFG; Weiss, Peletier, & Matteucci 1995, hereafter WPM). Within luminous elliptical galaxies, however, the magnesium-to-iron ratios are fairly constant (WFG).

WPM have made the first attempt at constructing stellar models of low-mass, high-metallicity stars with nonsolar abundance ratios. Magnesium and iron line strengths were synthesized by WPM and used to derive predicted giant elliptical galaxy [Mg/Fe] values between $+0.3$ and $+0.7$. While the total derived metal content is supersolar in these results, the iron metallicity is generally solar.

4. Although the interpretation is complex and the measurement is often complicated by emission, the Hβ line strength index has been used as an age indicator. Studies have found that, in the mean, the Hβ index is consistent with exhibiting no significant change in strength with radius (Davidge 1992; DSP; González 1993). Davies, Sadler, & Peletier (1993) concluded that their flat Hβ gradients imply no gradients in the age of the stellar population *within* individual ellipticals. Variations in the strength of the Hβ features *between* elliptical galaxies led González (1993) to suggest that significant differences exist in the ages of elliptical galaxies. Such age differences might be related to the presence of intermediate age components found in elliptical galaxies and bulges (see, e.g., Gilmore & van der Kruit 1995).

5. Although there have been suggestions that the sizes of galaxy line strength gradients are correlated with various photometric and kinematic properties, definitive trends have yet to emerge. From this sample of nearly 40 elliptical galaxies, González (1993) found that higher $\langle\sigma\rangle$ galaxies have shallower Mg and Fe gradients, while GES, Davidge (1992), and CDB found just the opposite correlation between velocity dispersion and the magnitude of Mg_2 gradients. González (1993) reported that velocity dispersion gradients are loosely correlated with line strength gradient sizes in the sense that steeper σ-gradient galaxies have steeper Mg metal gradients. From a sample of 11 bright elliptical galaxies, Davidge (1992) found a weak trend between Mg_2 gradients and $(V_m/\langle\sigma\rangle)^*$ in the sense that galaxies with steep Mg_2 gradients have more anisotropy than systems with shallower Mg_2 gradients. Davidge (1992) found that significant correlations do not exist between the magnitude of Mg_2 gradients and either central Mg_2, luminosity M_B, the Schweizer et al. (1990) fine-structure parameter Σ, or the fourth-order cosine isophote coefficient a_4.

The relationship proposed by Franx & Illingworth (1990, FI) between color gradients and escape velocity has been confirmed by DSP and CDB using the Mg_2 line strength indicator. Although this result suggests that line strength gradients and the color magnitude relation for elliptical galaxies arise from a common physical cause, the decoupling of Mg and Fe gradients and the spread in the relationship suggests that additional effects are present (DSP, CDB).

The work presented here addresses the above issues with a sample of seven elliptical galaxies and nine BCGs. There has been little published work on the line strengths of BCGs, and though there are indications that cD galaxies show different line strength behavior than elliptical galaxies (GES), previous sample sizes have been small. The main goal of the present study is to compare the stellar populations of BCGs to those of normal elliptical galaxies.

The paper is organized as follows. The two samples of objects selected for this study are discussed in § 2. Section 3 describes the reduction and analysis procedures as well as the stellar population models employed. The resulting line strengths and gradients are given in § 4. A discussion of the implications of these results is presented in § 5. The individual galaxies are represented in Figure 9. The Appendix provides the line strength results in tabular form.

2. SAMPLE SELECTION

The BCGs in this investigation are a subset of those studied kinematically in FIF. Four of the galaxies in the kinematic sample had redshifts which placed the line strength features of interest in the region of the bright night-sky lines Hg 5460 Å and [O I] 5577 Å. For these objects we could not derive accurate line strengths and they are not included in this study. The present sample contains the cD galaxies in Coma, and NGC 6166 in Abell 2199.

The elliptical sample consists of nearby, bright objects which have previously had their kinematics and line strengths studied by other investigators. These elliptical galaxies allow us to check our reduction and analysis procedures through a comparison of our derived measurements with those in the literature. Furthermore, since a primary aim of this study is to compare the stellar populations of early-type galaxies, the elliptical galaxies provide us with a consistently reduced, equivalent set of indices as for the BCGs. We are also in the process of studying the line strengths of a sample of S0 galaxies, which in conjunction with this investigation, will allow for a comparison of the stellar populations for a range of early-type galaxies.

Table 1 lists the objects studied in the present work. Individual notes detailing nonoptical properties, environmental factors, and the source of the Hubble type designation for each BCG can be found in FIF. Also listed in Table 1 are a number of structural and kinematic properties for the individual objects, as well as the velocity dispersion of the group or cluster that the object is associated with. With the exception of NGC 221, NGC 5831, and NGC 5846, all the kinematic parameters for the objects are from FIF. The kinematic results for these remaining three elliptical galaxies which are studied here, but not in FIF, were derived from our spectra in a manner identical to those for the other objects. We refer the reader to FIF for details concerning the kinematic measurements and determinations of r_e and $\sigma_{grp/cl}$.

3. DATA REDUCTION AND ANALYSIS

The long-slit spectra analyzed here were obtained at KPNO and Lick Observatory. Details of exposure times and slit positions are given in FIF. Reductions were carried out using the VISTA interactive image reduction package (Lauer, Stover, & Terndrup 1983). The detailed reduction procedures are described in FIF. The end product of these standard reduction techniques was a two-dimensional, geometrically rectified spectrum, binned logarithmically in the wavelength direction and linearly in the spatial direction. Described below are spe-

TABLE 1

GALAXY PARAMETERS

Galaxy	Type	M_B	r_e	ϵ	σ_o	$\frac{\Delta \log \sigma}{\Delta \log r}$	$(\frac{V_m}{\langle\sigma\rangle})^*$	$\sigma_{grp/cl}$
(1)	(2)	(3)	(4)	(5)	(6)	(7)	(8)	(9)
Ellipticals								
NGC 221	cE2	-15.43	36	0.26	80	-.067	1.12	...
NGC 2778	E	-21.00	16	0.28	168	-.152	1.29	142
NGC 4472	E2	-22.81	104	0.17	295	-.044	0.57	371
NGC 4649	E2	-22.36	74	0.15	360	-.087	0.65	664
NGC 5831	E3	-21.06	27	0.09	159	-.040	0.49	...
NGC 5846	E0	-22.68	63	0.07	229	-.013	0.28	125
NGC 7619	E	-22.27	32	0.22	325	-.100	0.41	253
Brightest Cluster Galaxies								
Abell 496	D	-23.16	54	0.16	272	-.027	0.25	681
NGC 2329	E	-22.69	24	0.15	234	-.064	1.07	444
NGC 2832	D	-23.18	30	0.20	320	-.073	0.12	629
NGC 4073	gE	-23.34	53	0.28	276	-.036	0.09	...
NGC 4839	cD	-22.66	43	0.51	288	-.010	0.04	945
NGC 4874	cD	-23.56	51	0.08	293	-.086	0.22	945
NGC 6166	cD	-24.13	48	0.26	295	-.064	0.08	801
NGC 7720	D	-22.98	38	0.19	337	-.129	0.09	822
NGC 7768	gE/D	-22.49	29	0.24	283	-.042	0.69	369

NOTES.—Col. (2) gives the galaxy types taken from the RC3 for the elliptical sample and from FIF for the BCG sample. The absolute blue magnitudes given in col. (3) were calculated from total apparent magnitudes given in Burstein et al. (1987) and from distances derived from Faber et al. (1989) using $H_0 = 50$ km s^{-1} Mpc^{-1}. The absolute magnitude for Abell 496 was taken from Peletier et al. (1990). Col. (4) lists effective radii in arcseconds, col. (5) gives ellipticities, $\epsilon = 1 - b/a$, and col. (6) gives the central stellar velocity dispersions as presented in FIF. The values for the major axis logarithmic gradient of velocity dispersion vs. radius given in col. (7) are taken from the kinematic study presented in FIF. In col. (8) we give the ratio of the observed maximum rotation velocity along the major axis to the average velocity dispersion within $r_e/2$. This ratio has been corrected for the effects of projection and ellipticity by normalization to the ratio expected for an oblate elliptical with isotropic velocity dispersion (see FIF). Col. (9) lists the velocity dispersions (in kilometers per second) for the groups or clusters of which the objects in this study are members (see Tables 3 and 4 of FIF).

cifics concerning the definition and measurement of absorption feature indices, corrections to the Lick–Image Dissector Scanner (IDS) system, and errors associated with our measured indices. We describe in § 3.5 the stellar models that we use for comparison with our derived line strengths.

3.1. *Definition and Measurement of Line Strength Indices*

The system of line strength indices originally defined by Faber et al. (1985) and slightly modified by González (1993) is used here. These indices are a result of a long-term program at Lick Observatory which initially used the IDS. A total of 21 spectral indices have been defined and measured in a large sample of stars, globular clusters, and early-type galaxies in order to study their stellar populations (Burstein et al. 1984; Faber et al. 1985; Burstein, Faber, & González 1986; Gorgas et al. 1993; WFG; González 1993).

Three wavelength regions need to be defined in order to measure a spectral index: an interval covering the feature of interest, and a pair of continuum bandpasses on each side of the feature. The strength of each spectral index is a measure of the flux in the central bandpass compared to a continuum level set by the sidebands. Indices are measured either as an equivalent width in angstroms (atomic indices) or as the ratio of line depth to continuum level in magnitudes (molecular indices).

The wavelength region covered by the observations obtained here contains the well-known magnesium triplet Mg *b*, as well as Hβ, and a number of iron lines. Table 2 lists the indices we study. Also given in Table 2 is a list of chemical elements (taken from Worthey 1993 and González 1993) present in each of the indices. It is apparent that most of the indices contain contributions from a variety of sources. The Fe5015 and Fe5270 indices contain contributions from Fe as well as from various iron-peak elements (i.e., Ni, Ti). Since these related elements owe their formation to processes similar to those forming Fe, the Fe5015 and Fe5270 indices are good indicators of "iron" abundance. The index Fe4668, however, contains a contribution from Mg I 4703 Å and is more realistically a combination Mg-Fe indicator rather than solely a diagnostic of iron abundance. Worthey (1993) mentions also that Fe4668 appears to contain C_2 and has found that the behavior of Fe4668 is more Mg-like than Fe-like in his models and in the Lick-IDS data.

TABLE 2

INDICES MEASURED

Index	Features	Bandpass	Blue sideband	Red sideband
Fe4668	FeI, CrI, TiI, MgI, NiI	4635.250–4721.500	4612.750–4631.500	4744.000–4757.750
Hβ	Hβ	4847.875–4876.625	4827.875–4847.875	4876.625–4891.625
Fe5015	FeI, TiI, NiI	4977.750–5054.000	4946.500–4977.750	5054.000–5065.250
Mgb	MgI	5160.125–5192.625	5142.625–5161.375	5191.375–5206.375
Fe5270	FeI, CaI	5245.650–5285.650	5233.150–5248.150	5285.650–5318.150
Fe5335	FeI, CrI, CaI, TiII	5312.125–5352.125	5304.625–5315.875	5353.375–5363.375

All the indices studied here are atomic indices. The molecular indices Mg_1 and Mg_2 were also measured, but they are not presented because they are susceptible to focus variations in the spectrum. Furthermore, the BCG redshifts frequently place their wide red sidebands in the region of the Hg 5460 Å night-sky line.

3.2. *Resolution Correction*

The first step in converting our line strength measurements to the Lick-IDS system is to account for the difference in spectral resolution between our data and the Lick-IDS data. The Lick-IDS system has a FWHM resolution of ~8.2 Å at ~5200 Å (González 1993). Since this is similar to the resolution of our KPNO data, no resolution correction was applied to the KPNO data. Our Lick data, however, have a FWHM resolution of ~3.2 Å at ~5200 Å and a transformation is needed to convert our indices to the Lick-IDS system.

Tests with stellar data have shown that the transformation to the Lick-IDS system from a different instrument is consistent with the relative resolution difference between the two (González 1993). Our resolution correction technique consisted of broadening our Lick spectra (at $\sigma_{\rm instr} = 75$ km s^{-1}) to the Lick-IDS resolution ($\sigma_{\rm IDS} = 200$ km s^{-1}) with a Gaussian filter. This broadening was done to our Lick data after the kinematics of the objects had been determined from a Fourier fitting program (described in FIF).

3.3. *Velocity Dispersion Correction*

A galaxy's stellar velocity dispersion weakens the strength of most of its absorption lines. To make comparisons of measured galaxy line strength indices with stellar models, corrections must be made to convert observed galaxy index values to those they would have if measured in a single star (i.e., $\sigma \simeq 0$). Additionally, since most elliptical galaxies have a radial gradient in their velocity dispersion it is necessary to know the *profile* of velocity dispersion in order to convert raw line strengths at measured radii into accurate gradients at a consistent zero point.

The technique used here to correct for velocity dispersion effects was to artificially broaden our stellar observations in order to derive empirical correction factors for each index. The index correction factors account for the decrease in measured line strength with increasing galaxy velocity dispersion. The size of the corection is typically small (less than 20% at $\sigma_{\rm gal} = 300$ km s^{-1}) for Hβ, Mg *b*, and Fe4668. Weaker lines, however, such as Fe5335, can have corrections to $\sigma = 0$ of ~40% at $\sigma_{\rm gal} \sim 300$ km s^{-1}.

For each instrument configuration (see FIF) the G-K giant stars used as velocity templates were broadened using a series of Gaussian filters from $\sigma = 0$ to $\sigma = 500$ km s^{-1} in 20 km s^{-1} increments. Each index was measured in each star over the entire range of broadening filters. Polynomial fits for each star were made, and an average set of correction factors were constructed for each instrument setup. The consistency among different stars within a run was generally very good. The scatter in the correction factors derived from different stars was typically $\lesssim 5\%$ for Mg *b* and $\lesssim 8\%$ for the Hβ and Fe indices. Since the corrections themselves are generally small, the scatter had negligible effect on the resulting indices. To save space, we do not show plots of the 18 correction factors employed here (six indices and three instrument configurations). Qualitatively, our correction factors are similar to those shown by DSP and González (1993).

Spectra were summed along the slit until a desired signal-to-noice ratio (S/N) was reached—typically S/N = 30–50 per pixel. A Fourier fitting routine fitted a broadened and redshifted stellar template to the binned galaxy spectra, and each binned row was de-redshifted. In our elliptical and BCG samples we found good agreement between the derived line strengths from the two sides of the nucleus for each object. Therefore, we added the spectra from the two sides of the nucleus at corresponding radii and derived index measurements from these higher S/N, co-added spectra.

The velocity dispersion profiles were fitted with a linear relation over the radial range of the binned spectra. Following this, our Lick data were broadened to the Lick-IDS resolution. Each index was measured on these de-redshifted and, for the Lick data, broadened galaxy spectra. Based on the linear fit to the velocity dispersion, the indices were transformed to a $\sigma = 0$ system with the empirical correction factors. With the resolution and velocity dispersion corrections completed, comparisons can now be made both among and within the galaxies in our sample with those in the Lick-IDS library.

3.4. *Error Analysis*

There are a variety of sources of error in line strength determinations. Instrumental systematics such as focus and response function variations, incorrect sky subtraction, and photon/read noise statistics can cause errors in line strength measurements. The measurement of weak absorption features is especially difficult, and is best overcome with high-resolution and high S/N observations from reliable equipment.

Our derived indices are relatively immune to large-scale variations in our spectra because we have limited ourselves to working only with atomic indices whose feature bandpasses and sidebands cover small spectral regions (compared with the molecular indices). The molecular index Mg_2 often suffers from the variable width of the instrument point spread function

perpendicular to the dispersion (i.e., focus variations). These variations in image size with wavelength distort the shape of spectra at small radii and cause errors in indices with large features and continuum bandpasses (González 1993). Our KPNO data which were obtained with the Cryogenic Camera are known to suffer from large-scale focus variations (see DSP and FIF), and some of our Lick data (that from the UV Schmidt camera) are also known to have focus problems. For this reason we have chosen the atomic index Mg *b* as our magnesium indicator rather than the more commonly used Mg_2.

As described in FIF, the sky level was determined from the outer parts of each galaxy frame. At each wavelength, a region ~ 50 pixels wide for the KPNO data and ~ 30 pixels wide for the Lick data, to either side of the galaxy nucleus, was linearly interpolated and subtracted. While this method has the undesirable effect of subtracting the portion of galaxy spectrum present at the slit ends, it has the benefit of accurately removing the true sky level in addition to removing smooth patterns of scattered light.

A number of tests were conducted to measure the effect of the contribution of galaxy light to the assumed sky level. The possible oversubtraction of light resulting from the determination of the sky level from the object frames was greatest for the calibrator galaxies because of their larger apparent sizes and higher surface brightnesses. The two galaxies in the elliptical sample which could be most effected by sky subtraction problems are NGC 4472, with a major axis $r_e = 114''$, and NGC 5846, with a major axis $r_e = 63''$. The data for NGC 4472 were obtained at KPNO with the Ritchey-Chrétien (RC) Spectrograph and a slit over 4′ long. The data for NGC 5846 were obtained at Lick with the Kast Double Spectrograph and a 2.′4 long slit.

Using CCD photometry by Peletier et al. (1990) for NGC 4472 and by Djorgovski (1985) for NGC 5846, surface brightness profiles of NGC 4472 and NGC 5846 were converted to the pixel scale used here and appropriately scaled for comparison with the profile integrated along the spectrum from 4700 Å to 5400 Å. For NGC 4472, the major axis spectrum was taken with the nucleus offset to one side of the slit. With the nucleus $\sim 15''$ from one end of the slit the sky level was determined from a region 193″–235″ away from the nucleus, where the galaxy surface brightness was 20% of the true sky level. For NGC 4472, the largest distance from the nucleus for which reliable line strengths could be measured was $\sim 57''$. For NGC 5846, the sky level was determined from rows 55″–70″ away from the nucleus, where the galaxy surface brightness was 18% of the true sky level. The largest distance from the nucleus for which reliable line strengths could be measured was 28″.

Because may of the galaxy observations had sky frames taken immediately before or after, it was possible to construct tests of the effects of galaxy contamination in the sky spectra that were taken from the edges of object frames. We scaled the independent sky frames so that when they were subtracted from our galaxy exposures the resulting integrated brightness profile from our spectra matched the independent CCD surface brightness profiles. In practice, the values derived from the frames that had the sky subtracted from their edges were found to be very similar (at the few percent level) to those derived from frames which had scaled independent sky frames subtracted, ie., no systematic errors apparently resulted from any residual galaxy component. Any difficulties with sky subtraction for the BCGs was reduced in comparison to the elliptical galaxies because the BCGS are more distant and have lower surface brightnesses. The contribution of galaxy light at the large radii where the sky levels were determined was found to be small ($\lesssim 5\%$). In summary, because line strengths are only measured to small radii and their gradients are generally shallow, the errors introduced by our sky subtraction procedure are minimal.

Another source of error in determining accurate line strengths for some of the indices is contamination by night-sky lines and emission intrinsic to the galaxy from warm gaseous components. We did not attempt to measure any index that had a skyline (e.g., Hg 5460 Å or [O I] 5577 Å) falling in one of its bandpasses. Thus, for none of our BCGs have we measured Fe5335, and only three have Fe5270 determinations.

Over a third of our total sample of objects (four BCGS and two Es) shows, at some level, emission from Hβ, and/or [O III] 4959 Å and [O III] 5007 Å. The indices most affected by this are the Hβ index and the Fe5015 index, which has [O III] 5007 Å in its feature bandpass. In the most severe cases emission lines can entirely fill in the absorption feature and cause the measured index to be negative. We have made no attempts to correct for this effect either theoretically, based on interstellar medium (ISM) predictions, or from an empirical standpoint. Rather, we present the indices as measured and make note of the existence of the emission.

3.5. *Modeling*

While no theoretical modeling was done on our part, we nonetheless wish to briefly discuss the models we adopted here for comparison with our observations. The stellar population models generated by Worthey (1994) are employed here. The motivation for line strength modeling is the fact that broad-band colors (and many indices) are incapable of distinguishing between the effects of age and metallicity in an integrated stellar population. Worthey has identified a number of indices which are claimed to break this degeneracy by being primarily sensitive to either age or metallicity and relatively immune to the other effect. One of the best age-sensitive indicators found by Worthey is Hβ, while the Fe4668 index is one of the more abundance-sensitive indicators.

The Worthey models assume that the horizontal branch (HB) lies in a red clump along the red giant branch. In this case, the Hβ feature is dominated by stars on the main-sequence turnoff, and the Hβ index can be used as an age discriminator. If, however, there exists a population of hot, yet old stars (i.e., a blue HB) then the use of Hβ as an age indicator is compromised (González 1993). There are indications that just such a populaton of hot, old stars exists in early-type galaxies. The models of Horch, Demarque, & Pinsonneault (1992) imply that low-mass, high-metallicity stars (2–3 times solar) can spend a significant amount of time (~ 20 Myr) in a "slow blue phase" which does not exist for less metal-rich stars.

Since the Worthey models are the most comprehensive treatment of line strength indices to date (21 indices are modeled), we use them with the understanding that further work is urgently needed concerning the late evolutionary stages of metal-rich stellar populations[5]. The single-burst models employed here by Worthey also need to be expanded

[5] The recent models developed by WPM lack the Hβ index and are limited to only the Mg_2 and $\langle Fe \rangle$ = (Fe5270 + Fe5335)/2 metal-line strength indices, neither of which is utilized in our study.

to include mixtures of stellar populations with varying abundances and multiple generations of star formation. The effects that secondary populations of different age and/or metallicity can have on measured line strengths need to be understood.

An additional issue involving the interpretation of the Hβ index concerns the dependence of HB evolution on the ratio of helium abundance to total metal abundance, $\Delta Y/\Delta Z$. The dependence of the relative enrichments $\Delta Y/\Delta Z$ on the slope of the initial mass function (IMF) at a given Z is such that flatter IMFs result in lower $\Delta Y/\Delta Z$ ratios (Maeder 1992). The reason for this is that more massive stars produce relatively more metals (Z) than helium (Y). As a result, the ratio $\Delta Y/\Delta Z$ declines as the IMF flattens. The behavior of the HB on $\Delta Y/\Delta Z$ is such that a decreasing helium to heavy element ratio causes the HB to become redder (Renzini 1993). Therefore, all things being equal, the flattening of an IMF results in a declining Hβ index.

Outstanding issues regarding the evolution of metal-rich populations include the determination of $\Delta Y/\Delta Z$, stellar mass loss, and opacities. The interpretation of the results presented here is limited by these and other uncertainties. In particular, the need to clarify the source(s) of the Hβ feature is paramount.

4. RESULTS

The derived Fe4668, Hβ, Fe5015, and Mg b line strength measurements for the elliptical and brightest cluster galaxies are shown in Figure 9. The results are presented in tabular form in the Appendix. Central magnesium line strength and global averages for all indices studied are presented in Table 3. Section 4.1 describes comparisons between the results derived for the seven elliptical galaxies from our sample and other authors. The analysis of our elliptical galaxy and BCG line strengths in terms of metallicities and ages are presented in §§ 4.2 through 4.4. Section 4.5 explores correlations between the sizes of our derived line strength gradients and various kinematic and dynamic properties of the individual galaxies. Section 4.6 describes the results concerning NGC 4073.

4.1. *Calibrator Galaxy Comparisons*

The derived Hβ, Fe5015, Mg b, Fe5270, and Fe5335 line strengths for our sample of seven elliptical galaxies are shown in Figure 9*a*. Also plotted are the corresponding measurements from González (1993), and for NGC 4472, the results of DSP. As can be seen from the figures, with a few exceptions, the agreement is generaly very good. However, there are a number of discrepant values indicating that the determination of accurate line strengths is still a challenging task. The index with the most discrepancy between our measurements and those of González (1993) is Fe5015. Measurement of the Fe5015 index can be complicated by the presence of [O III] 4959 Å emission in its blue sideband and [O III] 5007 Å emission in the feature bandpass.

We have binned our data to a fairly high S/N cutoff (S/N = 30–50) in order to obtain results which well constrain the line strength profile slopes. A drawback to this approach is that our profiles do not extend as far as they might were a lower cutoff used. From Figure 9*a* the relatively low scatter of our measurements can be compared with the González (1993) results which used a lower S/N cutoff and often extend to larger radii but show larger scatter. In comparison with our kinematic study, we have noticed that line strengths require higher S/N spectra in order to derive results of similar accuracy.

TABLE 3

LINE STRENGTHS

Galaxy	Mgb$_o$	Fe46	Hβ	Fe50	Mgb	Fe52	Fe53
(1)	(2)	(3)	(4)	(5)	(6)	(7)	(8)
Ellipticals							
NGC 221	2.91	4.82	2.27	5.37	2.93	3.00	2.69
NGC 2778	4.70	7.20	1.37*	5.30*	4.34	2.91	2.48
NGC 4472	5.02	7.18	1.49	6.19	4.78	3.06	2.63
NGC 4649	5.59	7.86	1.41	6.45	5.35	3.12	2.76
NGC 5831	4.33	5.96	2.15*	5.86*	3.89	3.15	2.80
NGC 5846	4.76	6.40	1.44*	5.60*	4.56	3.04	2.84
NGC 7619	5.37	7.40	1.69	5.53	4.87	3.10	2.83
Brightest Cluster Galaxies							
Abell 496	5.30	...	...	4.88*	5.18	...	...
NGC 2329	4.14	6.57	1.92*	4.91*	3.90	2.75	...
NGC 2832	5.04	8.10	1.41	5.43	4.78	2.92	...
NGC 4073	4.93	7.79	1.34	5.49	4.83	2.64	...
NGC 4839	5.02	6.93	1.42	4.52	4.68	...	...
NGC 4874	5.15	7.29	1.43	4.85	4.83	...	...
NGC 6166	5.31	6.45	1.23*	4.69*	4.49	...	...
NGC 7720	5.26	...	1.67*	5.34*	4.87	...	...
NGC 7768	4.66	...	1.34	5.17	4.44	...	...

NOTES.—Col. (2) gives the central magnesium strength, Mg b_0, within an aperture approximately 2″ × 4″ in size which covers the central ~1 kpc for an object at a distance of 50 Mpc. The central magnesium strengths for the more distant BCGs were determined through smaller sized apertures (~2″ × 2″) in order to correct for distance effects. The remaining columns give global averages (within $r_e/2$). Asterisks indicate the presence of emission lines which influence the measured indices.

4.2. *Central* Mg *b Line Strength versus* σ_0

The relationship between central magnesium strength and central velocity dispersion is a well studied correlation (see § 1). A direct physical explanation for the Mg-σ_0 relationship is complicated by the effects of age and metallicity on the stellar population indicator Mg b (or Mg_2) and the variety of processes influenced by σ_0 (see BBF). The Mg-σ_0 relation has been described as resulting from the increased level of enriched gas inflow in higher potential, higher σ_0 galaxies, thereby producing stars with higher metallicities (e.g., Larson 1976).

The relation between central magnesium strength, Mg b_0, and central stellar velocity dispersion, σ_0, is shown in Figure 1 for our sample of seven ellipticals and nine BCGs as well as 20 additional elliptical galaxies from the González (1993) sample. As with Mg_2, we find that Mg b_0 is well correlated with σ_0. The BCGs are seen to be in agreement with the relation followed by the elliptical galaxies. In conjunction with the BBF study, our results reinforce the conclusion that the Mg-σ_0 relation is a universal feature of early-type galaxies. A least-squares fit to the total sample gives the following relation: $\log \text{Mg } b_0 = 0.34\ (\pm 0.03) \log \sigma_0 - 0.11\ (\pm 0.07)$.

The scatter about the Mg b_0–σ_0 relation is real, and likely reflects a diversity in formation processes (BBF). No trends were found between the residuals about the mean relation and various kinematic parameters of the objects (σ_0, $[V_m/\langle\sigma\rangle]^*$, $\Delta \log \sigma/\Delta \log r$), parent cluster velocity dispersion, or Hβ line strength. This agrees with previous studies which also have not found strong correlations between the residuals from the Mg_2-σ_0 relation and photometric, kinematic, or fundamental plane parameters (e.g., BBF).

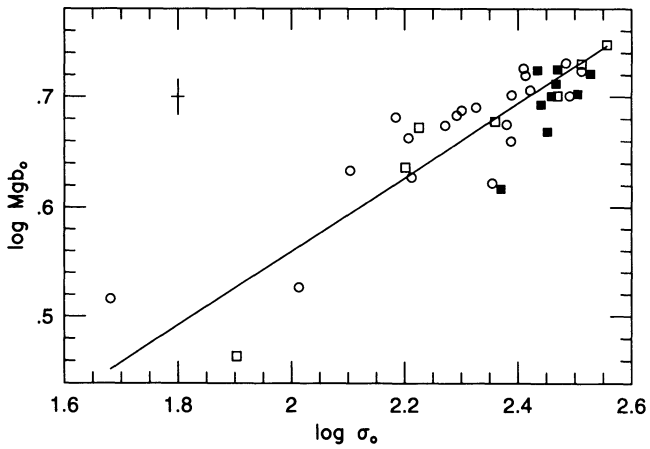

FIG. 1.—Logarithm of central Mg b index plotted against logarithm of central velocity disperson, σ_0. The seven ellipticals are shown as open squares, and the nine BCGs are shown as filled squares. Also shown are 20 additional ellipticals (*open circles*) from González (1993). A typical set of error bars is shown. The scatter is real. A double-regression fit to the total sample gives the relation shown as a solid line: log Mg $b_0 = 0.34\,(\pm 0.03)\log\sigma_0 - 0.11\,(\pm 0.07)$.

4.3. *Magnesium and Iron Ratios and Gradients*

Because of interference from skylines, the iron indices Fe5270 and Fe5335 were difficult to measure in our BCGs. Only three of our BCGs have redshifts low enough for the Fe5270 index to be determined without skyline contamination in either the feature bandpass or sidebands. The Fe5335 index in all nine of the BCGs was contaminated by either Hg 5460 Å or [O I] 5577 Å and could not be determined. Observations made at higher resolution are needed to avoid the skyline problems encountered here. Measurement of the iron index at 5406 Å would also be useful to better constrain the iron abundances of BCGs.

In Figure 2 we plot the measured magnesium Mg b and iron Fe5270 line strengths as well as the internal gradients for each object as determined by a least-squares fit to the data (see individual galaxy plots in Fig. 9). The gradients *within* elliptical galaxies and BCGs are seen to be in rough agreement with the model predictions (i.e., [Mg/Fe] ≈ constant), confirming results found earlier by WFG for their elliptical galaxy sample. A notable exception to the constant internal [Mg/Fe] ratio is M32, which displays a flat Mg b profile to the limit of our measurements but a Fe5270 gradient which results in an increase of the [Mg b/Fe52] ratio from 0.93 in the nucleus to 1.01 at the limit of our measurements (~22″).

Between galaxies, the iron abundances display only moderate variations and are not correlated with central velocity dispersion. Similar behavior in the iron indices was also noted by WFG for their elliptical galaxy sample and, compared to the wide variation in Mg abundance, indicates that Mg and Fe production mechanisms are decoupled. The increase in magnesium abundance with velocity dispersion and the corresponding lack of iron abundance variation with σ_0 dictates that more massive galaxies have larger [Mg/Fe] ratios than less massive ones. This behavior is apparent in Figure 3, where the ratio of the central Mg b amd Fe5270 indices is plotted.

In Figure 9b we show the sizes of the Hβ, Mg b, Fe5015, and Fe4668 gradients for each object. We find that our elliptical galaxy and BCG samples have similar average Mg b and also similar average Fe4668 gradients. The mean relations for both elliptical galaxies and BCGs are Δ log Mg b/Δ log $r = -0.06 \pm 0.02$ and Δ log Fe4668/Δ log $r = -0.11 \pm 0.02$. Taking the models literally, both of these gradients imply that Δ [Fe/H]/Δ log $r = -0.25 \pm 0.1$ at constant age, or a reduction in mean metallicity of the stellar population by a factor of ~2 over a factor of 10 in radius.

A number of investigators have used the Mould (1978) calibration to convert color and line strength gradients into [Fe/H] gradients. This method assumes that the radial change in these gradients is due to metallicity changes alone. Davies et al. (1993) calculated a metallicity gradient basd on their Mg_2 gradients of Δ[Fe/H]/Δ log $r = -0.23 \pm 0.09$, GES calculated Δ[Fe/H]/Δ log $r = -0.22 \pm 0.10$, and CH found Δ[Fe/H]/Δ log $r = -0.25$. The consistency between our study and these others is noteworthy and indicates that abundance gradients throughout the elliptical sequence are similar.

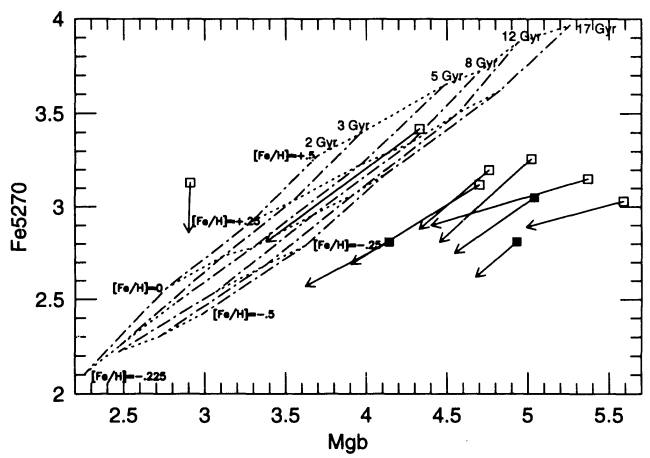

FIG. 2.—Iron Fe5270 index vs. Mg b. Symbols are located at the nuclei of the galaxies (*filled squares* for the BCGs and *open squares* for the ellipticals), and arrows show the last points measured. Overlain is the model grid of Worthey (1994) for single-burst populations. Compared to the models, magnesium is overabundant with respect to iron. While the slope of the Fe-Mg relation between galaxy nuclei is shallower than the model predictions, the fits to the internal gradients are similar to the model values (i.e., [Mg/Fe] ≈ constant). The data at Mg b = 2.9 Å are M32.

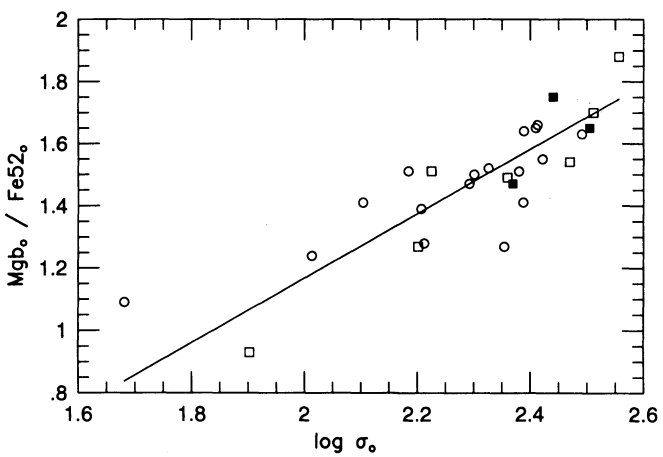

FIG. 3.—Central magnesium-to-iron ratio vs. central velocity dispersion. Symbol types are as in Fig. 1. The increase of [Mg/Fe] with elliptical galaxy mass is clearly seen. The data have been fitted with the relation Mg b_0/Fe $52_0 = 1.03\,(\pm 0.11)\log\sigma_0 - 0.90\,(\pm 0.27)$.

The derived line strengths for the BCGs presented here are limited to the central regions of the objects—typically extending to a few tenths of an effective radius. Line strength measurements at large radii are difficult because of the low surface brightnesses of the objects. Photometric measurements extending to $\gtrsim 1r_e$ of the MgH absorption band using medium bandwidth filters have been made for two of the galaxies in the present sample: NGC 4874 (Baum, Thomsen, & Morgan 1986) and NGC 4839 (Thomsen & Baum 1989). A comparison with our measurements presented here shows qualitatively that the large radii magnesium behavior of these objects is similar to the gradients found for the central regions i.e., the gradients are shallow.

4.4. *Ages and Metallicities*

Emission features present a problem in the determination of the Hβ index. Because a number of our elliptical galaxies and BCGs have central emission we characterize all the objects in our study with their average Hβ values. For galaxies with emission contamination, these ⟨Hβ⟩ strengths are taken from radii where we believe that emission is not affecting our measurements. However, for some galaxies our large radii values still might contain emission. For these objects (e.g., NGC 2778, Abell 496, NGC 7720) further observations to obtain results at larger radii or the use of higher order hydrogen features are needed.

The strength of the [O III] 5007 Å line is used as a diagnostic for the presence of emission. In the Appendix we tabulate the line strength results for each object and give a measure of the [O III] 5007 Å strength. The [O III] 5007 Å feature is determined in the same manner as other line strengths (i.e., with a defined bandpass and sidebands, measured with respect to the continuum level as an equivalent width in angstroms).

Figure 4 presents the central Mg *b* to Fe5270 ratio plotted against the average Hβ values. A strong correlation is found: objects with lower ⟨Hβ⟩ have higher Mg b_0/Fe52$_0$ ratios. Such a relation was totally unexpected. We note that the sample of González (1993) satisfies the same relation. No other parameters were found that correlate this strongly with Mg b_0/Fe52$_0$. For example, the correlation with σ_0 and M_B is weaker. We fit

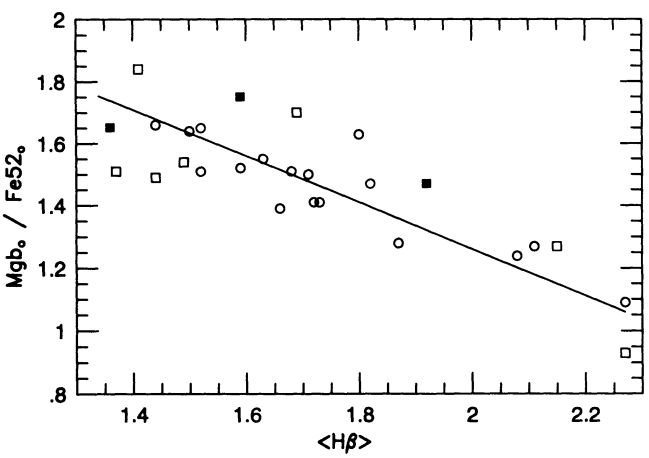

FIG. 4.—Central magnesium-to-iron ratio vs. average (within $r_e/2$) Hβ line strength. Symbol types are as in Fig. 1. A tight correlation is seen in the sense that galaxies with higher levels of Mg to Fe enhancement have correspondingly lower Hβ values. A fit to the data gives the relation Mg b_0/Fe52$_0$ = $-0.75(\pm 0.08)\langle H\beta\rangle + 2.75(\pm 0.14)$.

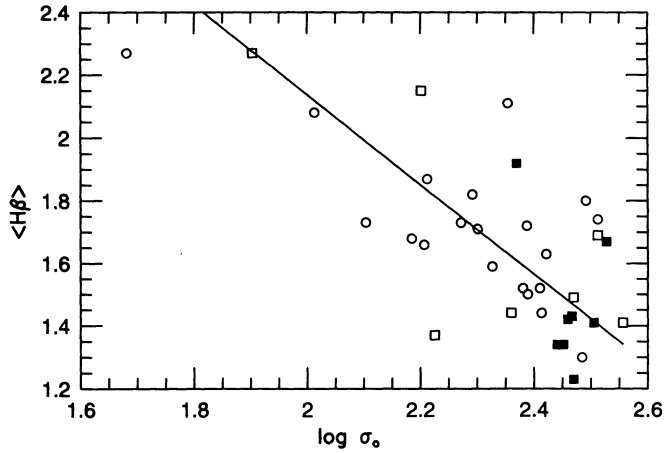

FIG. 5.—Average (within $r_e/2$) Hβ line strength vs. central velocity dispersion. Symbol types are as in Fig 1. A trend is apparent toward higher σ_0 galaxies having lower Hβ strengths. A fit to the data results in the relation $\langle H\beta\rangle = -1.43(\pm 0.19) \log \sigma_0 + 4.99(\pm 0.46)$.

a line and find a relation, Mg b_0/Fe52$_0$ = $-0.75(\pm 0.08)\langle H\beta\rangle + 2.75(\pm 0.14)$, with a scatter of $\sigma = 0.12$.

Most elliptical galaxies show fairly constant [Mg *b*/Fe52] ratios with radius (e.g., WFG, DSP, and § 4.3) and Hβ gradients are similarly shallow (see below). The difficulty of making observations which determine these shallow [Mg *b*/Fe52] and Hβ gradients with precision makes a similar study of the internal [Mg *b*/Fe52]–Hβ trend difficult. Therefore, the [Mg *b*/Fe52]–Hβ relation *within* elliptical galaxies is not as apparent as the relation between elliptical galaxies. Higher S/N observations would be of interest in elucidating the relationship between [Mg *b*/Fe52] ratio and Hβ within galaxies.

If the Hβ index can be interpreted as an age indicator, then this relation indicates that galaxies with higher magnesium-to-iron ratios are older than objects with lower [Mg b_0/Fe52$_0$]. Alternatively, if the Hβ index is due to blue HB stars, then the observed trend points toward IMF variations as the source of the correlation. These issues are discussed in § 5.

Figure 5 plots the average Hβ values versus central velocity dispersion. A weak trend is apparent toward more massive galaxies having lower Hβ line strengths. Similar behavior was noted by González (1993) with a corresponding large scatter in the correlation. If the Hβ index reflects the mean age of the stellar population, then at face value the observed trend would predict that more massive elliptical galaxies are, on average, older than less massive elliptical galaxies. Conversely, if the Hβ index is a feature of the HB, then the trend would suggest more massive elliptical galaxies have flatter IMFS than less massive galaxies.

In Figure 6 we plot our observed Hβ and Mg *b* values along with the Worthey model grid for single-burst populations. González (1993) was the first to show such a diagram and concluded that elliptical galaxies show a spread in ages that roughly correlates with their abundances in the sense that high-σ_0, metal-rich galaxies are older (~12–15 Gyr) than low-σ_0, weak-lined galaxies (~4–6 Gyr).[6] A primary result of the current investigation is the observation that, with the exception of NGC 2329 and NGC 7720, the BCGs populate the higher metallicity–lower Hβ region of the Mg *b*–Hβ plane.

[6] González (1993) also used Worthey models, and therefore his results are subject to the same cautions mentioned here.

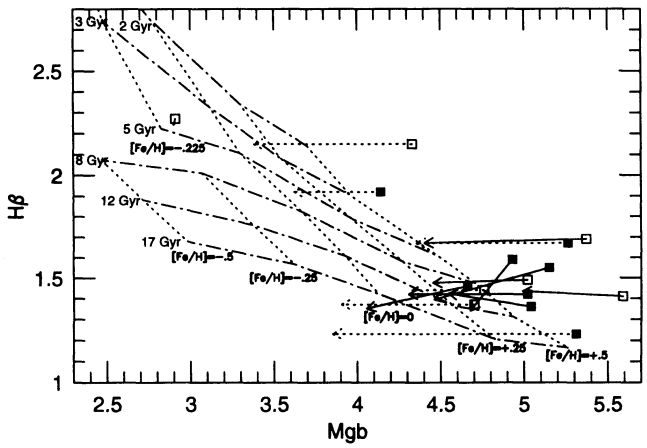

FIG. 6.—Compared model tracks and the measured Hβ and magnesium gradients. Symbols are located at the nuclei of the BCG (*filled squares*) and elliptical (*open squares*) galaxies, and arrows show the last points measured. A number of the objects show emission, which complicates the measurement of Hβ absorption. For these galaxies, we show their Hβ gradients as constant (*dotted lines*) at the average value (within $r_e/2$). Note that for the galaxies whose Hβ features were not contaminated by emission, the gradients are quite shallow. No significant differences are apparent in the sizes of the Mg *b* gradients for elliptical galaxies vs. BCGs. Overlain is the model grid of Worthey (1994) for single-burst populations. The two BCGs with central activity, NGC 2329 and NGC 7720, have high Hβ values which suggest young ages (Hβ = 1.92 and Hβ = 1.67 respectively).

The two BCGs NGC 2329 and NGC 7720 display Hβ line strengths which indicate young ages for these objects (~3 and ~5 Gyr, respectively). Both of these objects display extended Hβ and [O III] 5007 Å which might be excited by an active nucleus and/or current star formation. The galaxy NGC 2329 is the dominant member of a poor, low-velocity dispersion cluster. The luminosity of NGC 2329 is the lowest in our BCG sample and the galaxy displays a surface brightness profile typical of a normal elliptical (i.e., $r^{1/4}$ with no extended halo, see FIF). A wide-angle–tail (WAT) radio source has been identified with NGC 2329, and the galaxy displays significant rotation (Feretti et al. 1985). Multiple nuclei are present in NGC 7720, which is the central dominant galaxy in the X-ray cluster Abell 2634, and the WAT radio source 3C 465 has been identified with NGC 7720. It is possible that our measurements of NGC 2329 and NGC 7720 do not extend beyond the central active regions which presumably give rise to the high Hβ strengths. Further observations to larger radii would be valuable in order to investigate the underlying, and presumably older, population.

In Figure 6 we also show the gradients of Hβ and Mg *b* as determined from our fits to the observed data. The Hβ gradients for objects whose Hβ feature was contaminated by emission are shown as constant (*dotted lines*). For objects whose Hβ features were not contaminated by emission, we find that the measured Hβ profiles of both the elliptical galaxies and BCGs are consistent with no change with radius. Constant Hβ line strength with radius has also been found by other authors (see § 1). Excluding elliptical galaxies whose Hβ strengths cannot be reliably determined due to emission contamination, a large body of data (~50 Es) indicates that normal bright elliptical galaxies have relatively flat Hβ gradients.

In the presence of a metallicity gradient, constant Hβ strength translates into a shallow age gradient in the sense that our elliptical galaxies and BCGs have younger centers. As seen in the model grid, a constant age population displays a *rising* Hβ profile with radius in the presence of a declining metallicity gradient. The age gradient within an individual galaxy is not large, ~1–3 Gyr. Although care should be taken in making comparisons with the models on a galaxy by galaxy basis, taken as a whole our data suggest that BCGs have central ages ~8–12 Gyr, with outer parts being ~25% older. Similar results were reported by González (1993). These numbers are to be taken with caution until the models can be improved (with nonsolar abundance ratios, HB evolution, etc).

4.5. *Line Strength Gradient Trends*

In a dissipative formation scenario, galaxy line strength gradients should be well correlated with a variety of kinematic observables. Objects which converted gas to stars quickly, before the formation of a disk, would be kinematically hot (i.e., low values of $[V_m/\langle\sigma\rangle]^*$), have small velocity dispersion gradients, and have shallow abundance gradients. Galaxies which underwent more dissipation would have converted their gas to stars more slowly, and the opposite trends would emerge. As discussed in § 1, no strong correlations have been found linking line strength gradients to kinematic or structural properties. This suggests that a variety of mechanisms are present in elliptical galaxy formation and evolution.

In Figure 7 we plot our observed Mg *b* line strength gradients, $\Delta \log \mathrm{Mg}\ b/\Delta \log r$, versus a variety of parameters of the galaxies and their parent group/clusters. There might be a weak tendency for galaxies with steep velocity dispersion gradients to have correspondingly steep Mg *b* gradients, but the effect is not statistically significant in our data. A similar correlation between velocity dispersion gradients and line strength gradients was found by González (1993). This trend is in the direction expected if dissipational plays a role. No other trends are seen. Davidge (1992) did not find a correlation between Mg_2 gradients and either isophotal shape or the Schweizer et al. (1990) fine-structure parameter, Σ. A main conclusion found by CDB for their sample of elliptical galaxies was that for lower mass ($<10^{11}\ M_\odot$) galaxies, the Mg_2 gradients increase with increasing mass. More massive galaxies did not show a dependence on their gradient sizes. As our samples are biased toward massive objects, we cannot comment on such a trend, but we do confirm the lack of gradient correlations for massive galaxies.

4.6. *NGC 4073*

In our study of the kinematics of BCGs we found that NGC 4073, the dominant member of the poor cluster MKW 4, contains a counterrotating stellar core. The kinematics show that the core has a lower velocity dispersion than the main body of the galaxy, suggestive of a dynamically colder system. Such a subsystem could have been formed either during the initial collapse or because of a later merger.

In Figure 8 we plot our observed Hβ and Mg *b* line strengths for NGC 4073 and reproduce the kinematics from FIF. We find a ~0.5 Å increase in the Hβ strength at the center of NGC 4073, suggestive of either the accreted system being composed of younger stars or that star formation followed the accretion event. No emission lines are found in our spectrum of NGC 4073, indicating that no large-scale star formation is currently occurring in the system.[7] The sharp drop in Hβ strength with radius is evident in Figure 6, for which the models suggest that

[7] In Figs. 4 and 5 we show the Hβ measure for NGC 4073 taken at large radius—away from the kinematically distinct core.

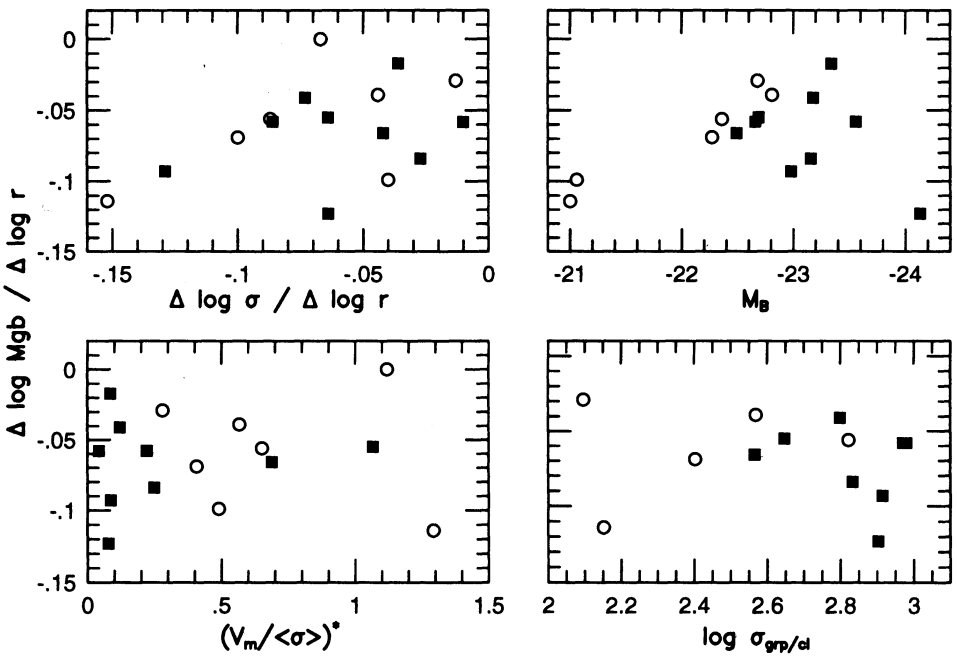

FIG. 7.—Individual Mg *b* gradients vs. various galaxy parameters. Compared with the elliptical galaxies, the BCGs have lower dimensionless rotation, $(V_m/\langle\sigma\rangle)^*$.

the age difference between the central and outer regions of NGC 4073 is substantial (Δage ~ 5–8 Gyr).

Davies et al. (1993) found that for two galaxies, NGC 4472 and NGC 7626, which both have kinematically distinct nuclei, the radial profiles of the Mg_2 strength show a steepening in the inner few arcseconds. In another study of elliptical galaxies with counterrotating stellar cores, Carollo & Danziger (1994a) found that NGC 2434 and NGC 7192 also display enhanced Mg_2 in the central regions. If the cause of these counterrotating components is from the merging of low-luminosity disks or compact elliptical galaxies, then one would expect that the central stellar populations should be metal-poor (Forbes,

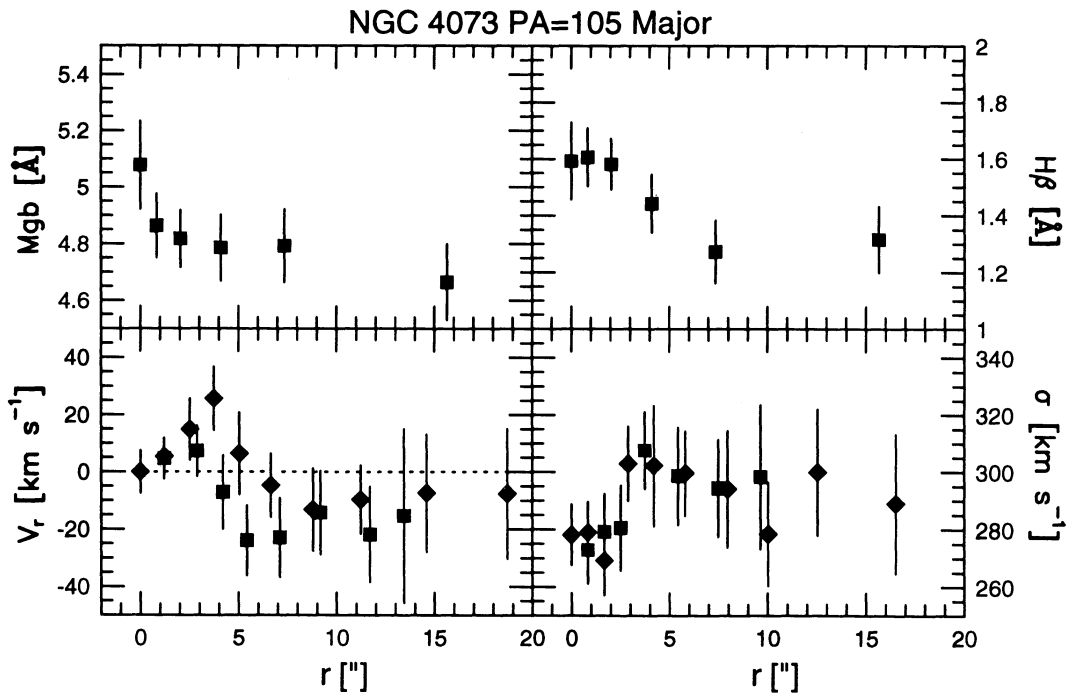

FIG. 8.—Line strengths and kinematics for the counterrotating core galaxy NGC 4073, the dominant member of the poor cluster MKW 4. The lower central velocity dispersion and rotation suggest that the accretion has resulted in a disk-like component. The enhanced Hβ strengths found in the central regions of the galaxy are indicative of either recent central star formation (although no emission is present) or the accreted object being a younger system.

Franx, & Illingworth 1994). However, this has generally not been observed (Franx & Illingworth 1988, 1990; Bender & Surma 1992).

A small increase in the central magnesium strength compared to larger radii is also observed in NGC 4073. From Figure 8, the nuclear Mg b line strength of NGC 4073 shows an increase of $\sim$0.2–0.3 Å with respect to the neighboring values at larger radii. However, the overall logarithmic Mg b gradient for NCG 4073 is shallow. With the exception of M32, NGC 4073 exhibits the smallest Mg b gradient for our sample. If the underlying main body of NGC 4073 is typical of other luminous elliptical galaxies, then a Mg b gradient would be expected. One possibility is that the counterrotating component has diluted the Mg b index in the inner regions through a combination of younger age and/or lower metallicity. The [Mg/Fe] ratio for NGC 4073 changes little with radius in contrast to the large change in Hβ.

5. DISCUSSION

In our kinematic study of BCGs we found that the velocity dispersion gradients BCGs and elliptical galaxies are similar. The BCGs were also found to be in agreement with studies showing the declining importance of rotation with increasing luminosity for elliptical galaxies (e.g., Davies et al. 1983). BCG mass-to-light (M/L) ratios derived from photometric and kinematic modeling were found to be within the range of M/L values occupied by elliptical galaxies. Thus, a primary conclusion of our kinematic investigation was that BCGs and elliptical galaxies share basic similarities in their internal stellar dynamics.

In the present study, two of the main results are that BCGs obey the same Mg b_0-σ_0 relation followed by elliptical galaxies and that BCGs have similar metal line strength gradients as elliptical galaxies. These results, in conjuncton with the findings from our kinematic study, are evidence that BCGs are the natural high-luminosity extension of the elliptical sequence, implying that the formation and evolutionary histories of BCGs and elliptical galaxies were similar. Further work is needed to investigate whether the low-luminosity end of the elliptical sequence shares in the continuity found here for normal elliptical galaxies and BCGs. We note that both our kinematic and line strength conclusions apply only to the main bodies of BCGs and *not* the extended halos, which we did not measure.

The observations presented here confirm previous findings that elliptical galaxies display a trend of increasing [Mg/Fe] ratio with increasing galaxy velocity dispersion and hence mass (e.g., WFG; Carollo & Danziger 1994a). Combinations of age and metallicity based on scaled solar abundance ratios are not able to reproduce either the mean [Mg/Fe] values in individual galaxies or the shallow slope between objects (WFG). Observations of Galactic metal-rich stars are needed to investigate the possibility of abundance ratio variations, and improved models are needed to better understand the behavior of stars at high metallicity.

Because Mg and Fe are produced from different types of supernovae (Type II vs. Type Ia), WFG suggested three possible scenarios that could explain the variation of [Mg/Fe] among elliptical galaxies: (1) different star formation timescales, (2) a variable IMF, and (3) selective mass loss. Matteucci (1994) verified that scenarios (1) and (2) do indeed produce the observed trend using a chemical evolution model for elliptical galaxies.

In the first scenario, the observed increase in [Mg/Fe] ratio with increasing galaxy mass is due to enhanced star formation efficiency. The [Mg b_0/Fe52$_0$]–Hβ relation is not predicted by this scenario. Hence, changes in the Hβ index are likely due to age and would imply that more massive elliptical galaxies formed quicker *and earlier* than less massive elliptical galaxies. This follows from the fact that a change in the rate of star formation would not significantly affect the ratio $\Delta Y/\Delta Z$, and thus the Hβ index would not be altered. Yet the clear trend of Hβ with [Mg b_0/Fe52$_0$] would still require an explanation with age being the most obvious answer. In this case, more massive elliptical galaxies would on average be older than less massive elliptical galaxies, although interactions, cooling flows, and other mechanisms could still produce varying levels of continued star formation.

If Hβ can be used as an age indicator, then a number of conclusions follow from our findings. That the Hβ line strengths of the objects in our sample span a range of values would suggest that significant age differences exist among the elliptical family. Similar results have been seen in the past. Though it is recognized that the stellar populations of luminous elliptical galaxies are generally old, differences in age among elliptical galaxies have been shown. In the well-studied case of M32, the presence of an intermediate-age component has been established (O'Connell 1980; Burstein et al. 1984; Rose 1985; Bica, Alloin, & Schmidt 1990; Elston & Silva 1992; Freedman 1992; González 1993). The BCG sample generally has low global Hβ line strengths, which on the basis of Worthey's models predicts that the bulk of these systems underwent their last episode of star formation $\gtrsim$8–10 Gyr ago.

If the second of the three WFG scenarios is correct, and a variable IMF in elliptical galaxies is the answer, then both the observed [Mg/Fe] and Hβ behavior may be accounted for. An IMF which is flatter for more massive galaxies would give the observed trend of [Mg/Fe] with σ_0 and might also produce the Hβ behavior, as flatter IMFs produce lower $\Delta Y/\Delta Z$, redder horizontal branches, and lower values of Hβ. In this case, elliptical galaxy ages could span a relatively small range of values, and the Hβ index would be a consequence of the color spread in HB populations.

Quantitative predictions from the last of the WFG scenarios (selective mass loss) are not presently available. The difficulty in making accurate observations of mass-loss phenomena and the general lack of knowledge concerning the detailed physical processes of supernovae and stellar winds make the topic of mass loss hard to address.

In summary, our findings are not able to decisively discriminate between the validity of the various possible scenarios but point to the need for further study in the area of IMFs, HB evolution, and other methods for age estimation. Mass-loss rates and helium abundances, both of which are difficult to constrain observationally and act as free parameters in current models, can have dramatic effects on predicted Hβ strengths (see Dorman, Rood, & O'Connell 1993). Also of interest is a possible connection between the UV light in elliptical galaxies and its relation to the Hβ line. The correlation between $1550 - V$ color and Mg$_2$ strength is possibly an important link between the stellar components in these systems (Wu et al. 1980; Faber 1983; Burstein et al. 1988; Ferguson & Davidsen 1993). Further work is urgently needed to clarify the source(s) of the Hβ feature.

The effect of emission lines on the Hβ index is another serious concern. Since the presence of emission on line strength

indices is to fill in the features and cause lower values to be measured, there is the possibility that the low Hβ levels found for our BCGs are caused by emission-filled Hβ. However, with the use of the [O III] 5007 Å line as an emission indicator, we have confidence that the low Hβ values in our BCGs are a real effect. Another solution is to obtain measurements of higher order Balmer lines which are less prone to gaseous emission. Future observations of the Hγ, Hδ, and the G4300 (G band) indices will enable more accurate age determinations to be made.

For galaxies whose Hβ feature was not effected by emission, we find that the Hβ gradients are consistent with being flat. Flat Hβ gradients predict that the centers of the elliptical galaxies and BCGs are younger by $\sim$1–3 Gyr than the outer regions. These findings suggest that a variety of galaxy formation scenarios should be considered, including those having denser stellar components forming at late times. A merger origin for elliptical galaxies and BCGs might account for our observed age gradient if the inflow of accreted gas was followed by star formation at the galaxy centers.

If elliptical galaxies form purely by dissipational collapse, then they should have steep abundance gradients and a trend toward more massive elliptical galaxies having the steepest gradients (Larson 1976; Carlberg 1984). Conversely, a purely stellar merger origin for elliptical galaxies produces no metallicity gradients. No strong correlations between line strength gradients and either photometric or kinematic galaxy parameters were found for our sample. Thus, the spread in gradient sizes likely reflects a corresponding diversity in star formation histories for elliptical galaxies (GES; Davidge 1992; DSP).

D. F. thanks J. González for providing VISTA procedures and useful discussions. We also thank G. Worthey for discussions and providing the model grid. M. F. acknowledges support by Hubble Fellowship grant HF-1016.01.91A and the Harvard Society of Fellows.

This research has made use of the NASA/IPAC Extragalactic Database (NED), which is operated by the Jet Propulsion Laboratory, Caltech, under contract with the National Aeronautics and Space Administration.

APPENDIX

DATA TABLES

The Fe4668, Hβ, Fe5015, and Mg *b* line strength results are tabulated for the entire sample of observations (see Tables 4 and 5 and Figure 9, following the References). All line strengths are velocity dispersion corrected and calibrated to the Lick-IDS system. Also given are measures of the [O III] 5007 Å emission line. The effective radius along the observed axis is given for each object.

REFERENCES

Baum, W. A., Thomsen, B., & Morgan, B. L. 1986, ApJ, 301, 83
Bender, R., Burstein, D., & Faber, S. M. 1993, ApJ, 411, 153 (BBF)
Bender, R., & Surma, P. 1992, A&A, 258, 250
Bertola, F., Burstein, D., & Buson, L. 1993, ApJ, 403, 573
Bica, E., Alloin, D., & Schmidt, A. A. 1990, A&A, 228, 23
Boroson, T. A., & Thompson, I. B. 1991, AJ, 101, 111
Burstein, D., Bertola, F. B., Buson, L. M., Faber, S. M., Lauer, T. R. 1988, ApJ, 328, 440
Burstein, D., Davies, R. L., Dressler, A., Faber, S. M., Lynden-bell, D., Terlevich, R., & Wegner, G. 1988, in Towards Understanding Galaxies at Large Redshift, ed. R. G. Kron & A. Renzini (Dordrecht: Kluwer)
Burstein, D., Faber, S. M., Gaskell, C. M., & Krumm, N. 1984, ApJ, 287, 586
Burstein, D., Faber, S. M., & González, J. J. 1986, AJ, 91, 1130
Burstein, D., Davies, R. L., Dressler, A., Faber, S. M., Stone, R. P. S., Lynden-Bell, D., Terlevich, R., & Wegner, G. 1987, ApJS, 64, 601
Carlberg, R. G. 1984, ApJ, 286, 403
Carollo, C. M., & Danziger, I. J. 1994a, MNRAS, 270, 523 (CD)
———. 1994b, MNRAS, 270, 743
Carollo, C. M., Danziger, I. J., & Buson, L. 1993, MNRAS, 265, 553 (CDB)
Couture, J., & Hardy, E. 1988, AJ, 96, 867 (CH)
Davidge, T. J. 1992, AJ, 103, 1512
Davies, R. L., Efstathiou, G., Fall, S. M., Illingworth, G., & Schechter, P. L. 1983, ApJ, 266, 41
Davies, R. L., Sadler, E. M., & Peletier, R. F. 1993, MNRAS, 262, 650 (DSP)
Delisle, S., & Hardy, E. 1992, AJ, 103, 711
Djorgovski, S. 1985, Ph.D. thesis, Univ. of California
Dorman, B., Rood, R. T., & O'Connell, R. W. 1993, ApJ, 419, 596
Dressler, A. 1984, ApJ, 281, 512
Dressler, A., Lynden-Bell, D., Burstein, D., Davies, R. L., Faber, S. M., Terlevich, R. J., & Wegner, G. 1987, ApJ, 313, 42
Efstathiou, G., & Gorgas, J. 1985, MNRAS, 215, 37P
Elston, R., & Silva, D. 1992, AJ, 104, 1360
Faber, S. M. 1973, ApJ, 179, 423
———. 1977, in The Evolution of Galaxies and Stellar Populations, ed. B. T. Tinsley & R. B. Larson (New Haven: Yale Univ. Press), 157
———. 1983, Highlights Astron., 6, 165
Faber, S. M., Friel, E., Burstein, D., & Gaskell, C. M. 1985, ApJS, 57, 711
Faber, S. M., Wegner, G., Burstein, D., Davies, R. L., Dressler, A., Lynden-Bell, D., & Terlevich, R. 1989, ApJS, 69, 763
Feretti, L., Giovanni, G., Gregorini, L., Padrielli, L., Roland, J., & Valentijn, E. A. 1985, A&A, 147, 321
Ferguson, H. C., & Davidsen, A. F. 1983, ApJ, 408, 92
Fisher, D., Illingworth, G., & Franx, M. 1995, ApJ, 438, 539 (FIF)
Forbes, D. A., Franx, M., & Illingworth, G. D. 1994, ApJ, 428, L49
Franx, M., & Illingworth, G. D. 1988, ApJ, 327, L55
———. 1990, ApJ, 359, L41 (FI)
Freedman, W. L. 1992, AJ, 104, 1349
Gilmore, G., & van der Kruit, P., ed. 1995, IAU Symp. 164, Stellar Populations (Dordrecht: Kluwer)
González, J. J. 1993, Ph.D. thesis, Univ. of California
Gorgas, J., Efstathiou, G., & Salamanca, A. 1990, MNRAS, 245, 217 (GES)
Gorgas, J., Faber, S. M., Burstein, D., González, J. J. Courteau, S., & Prosser, C. 1993, ApJS, 86, 153
Horch, E., Demarque, P., & Pinsonneault, M. 1992, ApJ, 388, L53
Larson, R. B. 1976, MNRAS, 176, 31
Lauer, T. R., Stover, R. J., & Terndrup, D. 1983, Lick Obs. Tech. Rept. No. 34
Maeder, A. 1992, A&A, 264, 105
Matteucci, F. 1994, A&A, 288, 57
Mould, J. R. 1978, ApJ, 220, 434
O'Connell, R. 1980, ApJ, 236, 430
Peletier, R. F. 1989, Ph.D. thesis, Rijksuniversiteit Groningen
Peletier, R. F., Davies, R. L., Illingworth, G. D., Davies, L., & Cawson, M. 1990, AJ, 100, 1091
Renzini, A. 1993, in IAU Symp. 153, Galactic Bulges, ed. H. Dejonghe & H. J. Habing (Dordrecht: Kluwer), 151
Rose, J. A. 1985, AJ, 90, 1927
Schweizer, F., Seitzer, P., Faber, S. M., Burstein, D., Dalle Ore, C. M., & González, J. J. 1990, ApJ, 364, L33
Terlevich, R., Davies, R. L., Faber, S. M., & Burstein, D. 1981, MNRAS, 196, 381
Thomsen, B., & Baum, W. A. 1989, ApJ, 347, 214
Weiss, A., Peletier, R. F., & Matteucci, F. 1995, A&A, 296, 73 (WPM)
Worthey, G. 1993, Ph.D. thesis, Univ. of California
———. 1994, ApJS, 95, 107
Worthey, G., Faber, S. M., & González, J. J. 1992, ApJ, 398, 69 (WFG)
Wu, C.-C., Faber, S. M., Gallagher, J. S., Peck, M., & Tinsley, B. M. 1980, ApJ, 237, 290

TABLE 4

CALIBRATOR GALAXY DATA

r (″)	Fe46	ε	Hβ	ε	Fe50	ε	Mgb	ε	[OIII]	ε
NGC 221 (M32) PA=159 Major r_e=45″										
0.40	5.30	.11	2.33	.05	5.27	.11	2.95	.06	0.00	.03
0.80	5.06	.08	2.25	.04	5.31	.09	2.89	.05	0.00	.02
1.60	4.75	.10	2.30	.05	5.45	.10	2.92	.06	0.00	.03
2.40	4.93	.12	2.33	.06	5.54	.13	2.96	.07	0.00	.03
3.20	4.91	.14	2.27	.07	5.43	.15	2.98	.08	0.00	.04
4.36	4.84	.12	2.31	.06	5.41	.13	2.96	.07	0.00	.04
6.32	4.59	.13	2.27	.06	5.31	.13	2.94	.07	0.00	.04
9.09	4.68	.14	2.23	.07	5.30	.14	2.88	.08	0.00	.04
13.34	4.62	.15	2.26	.07	5.32	.15	2.94	.08	0.00	.05
22.09	4.50	.16	2.18	.07	5.31	.16	2.87	.09	0.00	.05
NGC 2778 PA=40 Major r_e=19″										
0.84	8.33	.12	1.49	.06	5.65	.15	4.75	.08	0.61	.04
1.99	7.12	.14	1.39	.08	5.47	.21	4.43	.10	0.51	.06
4.93	6.15	.17	1.24	.09	4.77	.23	3.83	.11	0.76	.06
NGC 4472 PA=155 Major r_e=114″										
0.84	8.22	.09	1.45	.04	6.72	.12	5.16	.06	0.00	.03
2.07	7.99	.07	1.51	.03	6.52	.09	5.00	.04	0.00	.02
3.75	7.74	.08	1.54	.04	6.38	.11	4.96	.05	0.00	.02
5.80	7.16	.08	1.47	.04	6.29	.11	4.81	.05	0.00	.02
8.71	6.90	.08	1.41	.04	6.08	.12	4.74	.05	0.00	.03
12.84	6.70	.09	1.53	.04	6.03	.12	4.83	.06	0.00	.03
19.37	6.18	.09	1.46	.04	5.93	.12	4.71	.06	0.00	.03
32.07	6.16	.09	1.50	.04	5.77	.12	4.52	.06	0.00	.03
56.56	5.71	.13	1.36	.06	5.71	.18	4.40	.09	0.00	.04
NGC 4472 PA=65 Minor r_e=95″										
0.84	8.59	.07	1.50	.03	6.74	.10	5.01	.04	0.00	.02
1.68	8.19	.07	1.58	.04	6.70	.10	5.10	.05	0.00	.02
2.91	7.93	.06	1.54	.03	6.72	.08	4.91	.04	0.00	.02
4.59	7.79	.07	1.47	.03	6.41	.10	4.84	.05	0.00	.02
6.64	7.58	.07	1.57	.03	6.21	.10	4.69	.05	0.00	.02
9.90	7.05	.07	1.47	.03	6.05	.10	4.68	.05	0.00	.02
15.57	6.54	.07	1.49	.04	5.70	.10	4.48	.05	0.00	.02
29.76	5.62	.07	1.49	.04	5.31	.10	4.34	.05	0.00	.02
NGC 4649 PA=105 Major r_e=80″										
1.68	8.97	.18	1.36	.08	6.97	.26	5.77	.12	0.00	.05
2.91	8.60	.13	1.37	.06	6.95	.20	5.77	.09	0.00	.04
4.59	8.44	.15	1.44	.07	6.91	.23	5.40	.11	0.00	.05
6.64	8.35	.15	1.48	.07	6.08	.22	5.35	.10	0.03	.05
9.55	8.10	.16	1.39	.08	6.63	.24	5.41	.11	0.00	.05
13.65	7.52	.17	1.38	.08	6.05	.25	5.24	.11	0.00	.05
21.39	6.99	.18	1.41	.08	6.23	.25	5.10	.12	0.00	.06
28.70	5.88	.31	1.45	.15	5.79	.43	4.73	.20	0.00	.10

TABLE 4—*Continued*

r (″)	Fe46	ε	Hβ	ε	Fe50	ε	Mgb	ε	[OIII]	ε
NGC 5831 PA=55 Major r_e=28″										
0.40	8.81	.22	1.87	.10	6.25	.20	4.46	.09	0.14	.05
0.80	8.03	.17	1.89	.07	6.33	.16	4.40	.07	0.05	.04
1.60	6.71	.22	1.90	.09	6.23	.20	4.08	.09	0.00	.05
2.40	5.30	.29	1.96	.12	5.84	.27	3.87	.11	0.09	.07
3.54	4.60	.29	1.98	.12	5.87	.25	3.60	.11	0.07	.06
5.50	4.15	.33	2.04	.14	5.42	.30	3.46	.13	0.09	.08
9.23	4.10	.36	2.15	.14	5.05	.31	3.39	.13	0.01	.08
NGC 5846 PA=73 Major r_e=65″										
0.40	7.52	.25	0.97	.13	5.26	.35	4.81	.16	0.57	.08
0.80	7.30	.18	0.98	.10	5.11	.25	4.68	.12	0.52	.06
1.60	6.95	.20	1.07	.11	5.20	.28	4.83	.12	0.38	.06
2.40	6.67	.22	1.24	.12	5.36	.31	4.67	.14	0.29	.07
3.20	6.71	.25	1.34	.14	5.42	.36	4.49	.16	0.08	.08
4.36	6.18	.21	1.18	.12	5.62	.30	4.69	.13	0.23	.06
5.97	6.59	.25	1.17	.13	5.44	.36	4.57	.16	0.18	.08
7.94	6.07	.25	1.34	.14	5.38	.34	4.40	.15	0.01	.08
11.05	5.95	.25	1.44	.13	5.72	.35	4.38	.15	0.07	.08
16.96	5.65	.25	1.40	.14	5.36	.37	4.38	.15	0.00	.08
27.06	4.68	.36	1.45	.20	5.75	.54	4.43	.21	0.00	.12
NGC 5846 PA=163 Minor r_e=61″										
0.40	7.31	.25	1.11	.14	4.96	.35	4.76	.16	0.51	.08
0.80	7.50	.18	1.11	.10	5.12	.25	4.78	.12	0.46	.06
1.60	7.07	.20	1.27	.11	5.72	.28	4.67	.13	0.31	.06
2.40	6.80	.23	1.41	.13	5.49	.32	4.66	.14	0.31	.07
3.56	6.37	.19	1.26	.11	5.64	.27	4.71	.12	0.10	.06
5.17	6.37	.24	1.27	.13	5.30	.34	4.63	.15	0.23	.08
7.14	6.29	.24	1.24	.12	5.25	.33	4.53	.15	0.27	.08
10.24	5.68	.25	1.32	.13	5.78	.35	4.52	.15	0.11	.08
16.29	5.53	.25	1.46	.14	5.17	.37	4.22	.15	0.00	.08
28.35	5.26	.36	1.53	.18	6.22	.51	3.86	.21	0.00	.12
NGC 7619 PA=28 Major r_e=36″										
0.42	8.40	.19	1.60	.08	5.88	.25	5.50	.11	0.00	.05
0.84	7.73	.13	1.82	.06	5.78	.18	5.15	.08	0.00	.04
1.68	7.31	.15	1.72	.07	5.94	.21	5.20	.10	0.00	.05
2.87	...	...	1.53	.07	5.82	.19	5.04	.09	0.00	.05
4.91	...	...	1.77	.08	5.45	.22	4.68	.10	0.00	.05
8.76	7.09	.16	1.64	.08	5.17	.23	4.33	.11	0.00	.06
11.89	6.46	.23	1.72	.12	4.70	.33	4.20	.16	0.00	.08

TABLE 5

BRIGHT CLUSTER GALAXY DATA

r (″)	Fe46	ε	Hβ	ε	Fe50	ε	Mgb	ε	[OIII]	ε
Abell 496 PA=176 Major r_e=59″										
0.33	...	...	...	...	0.79	.69	5.61	.49	3.20	.23
0.95	...	...	...	...	3.79	.55	5.16	.28	2.66	.13
2.67	...	...	...	...	3.77	.63	4.80	.31	1.93	.16
5.36	...	...	...	...	4.92	.74	3.94	.37	1.16	.21
Abell 496 PA=86 Minor r_e=49″										
0.33	...	...	...	...	3.90	1.61	5.38	.69	2.17	.32
0.95	...	...	...	...	3.05	0.86	5.06	.43	2.44	.18
2.79	...	...	...	...	3.68	0.88	4.60	.48	2.24	.22
4.20	...	...	...	...	5.87	1.49	4.75	.96	2.04	.37
NGC 2329 PA=175 Major r_e=26″										
0.40	7.70	.30	1.19	.12	3.48	.27	4.16	.12	0.41	.05
0.80	7.61	.22	1.27	.09	4.27	.20	4.23	.09	0.31	.04
1.60	7.06	.25	1.69	.10	4.75	.24	3.97	.10	0.10	.04
2.40	6.61	.30	1.93	.12	5.05	.30	4.03	.12	0.00	.05
3.54	6.48	.28	2.01	.11	5.31	.27	3.96	.11	0.00	.05
5.50	5.96	.32	1.67	.13	4.87	.30	3.92	.12	0.00	.06
9.22	5.31	.32	1.68	.13	4.33	.29	3.34	.12	0.00	.06
15.67	5.19	.50	2.15	.23	3.91	.43	3.21	.18	0.00	.10
NGC 2329 PA=85 Minor r_e=22″										
0.40	7.73	.27	1.21	.11	3.99	.23	4.17	.11	0.62	.05
0.80	7.51	.21	1.32	.08	4.43	.19	4.25	.08	0.36	.03
1.60	6.84	.25	1.69	.10	4.89	.23	4.07	.10	0.11	.04
2.40	6.15	.30	1.85	.12	4.96	.28	3.97	.12	0.00	.05
3.20	6.46	.37	1.95	.15	5.60	.38	3.91	.15	0.00	.07
4.00	6.43	.44	2.01	.18	5.59	.45	3.79	.17	0.00	.08
5.16	6.14	.40	2.01	.17	4.47	.39	3.79	.16	0.00	.08
7.11	5.99	.46	2.07	.19	5.20	.44	3.57	.17	0.00	.09
NGC 2832 PA=160 Major r_e=34″										
0.42	9.73	.32	1.42	.10	5.52	.26	4.99	.12	0.16	.05
0.84	8.89	.24	1.37	.07	5.80	.19	5.01	.09	0.07	.04
1.68	8.74	.26	1.42	.08	5.61	.22	5.20	.10	0.03	.05
2.52	8.30	.29	1.39	.10	5.38	.26	4.94	.11	0.09	.06
3.36	8.27	.32	1.46	.11	5.46	.30	4.81	.13	0.15	.07
4.20	7.87	.38	1.39	.13	5.41	.35	4.64	.16	0.00	.08
5.42	7.28	.33	1.51	.12	5.24	.30	4.36	.13	0.00	.07
7.47	6.88	.36	1.35	.13	5.38	.32	4.59	.15	0.00	.07
10.92	6.93	.40	1.39	.13	5.08	.35	4.46	.16	0.07	.08
NGC 4073 PA=105 Major r_e=62″										
0.42	8.54	.45	1.59	.14	6.11	.35	5.08	.16	0.08	.07
0.84	8.06	.32	1.61	.10	5.73	.26	4.86	.11	0.00	.06
2.04	7.90	.27	1.58	.09	5.57	.23	4.82	.10	0.00	.05
4.10	7.99	.30	1.44	.10	5.19	.27	4.79	.12	0.00	.06
7.36	7.59	.34	1.27	.11	5.25	.29	4.79	.13	0.03	.06
15.65	6.69	.36	1.32	.12	5.08	.31	4.66	.13	0.17	.07
NGC 4839 PA=65 Major r_e=61″										
0.42	7.70	.52	1.39	.16	4.87	.41	5.27	.18	0.20	.08
0.84	6.74	.38	1.45	.12	4.80	.30	5.13	.13	0.00	.06
1.68	7.27	.40	1.39	.14	4.77	.35	5.02	.15	0.00	.07
2.88	7.06	.34	1.55	.12	4.26	.30	4.58	.13	0.00	.07
5.25	6.51	.37	1.62	.13	4.06	.33	4.51	.14	0.05	.07
10.16	6.01	.49	1.35	.16	3.67	.43	4.16	.18	0.00	.09

TABLE 5—*Continued*

r (″)	Fe46	ε	Hβ	ε	Fe50	ε	Mgb	ε	[OIII]	ε
					NGC 4839 PA=155 Minor r_e=30″					
0.42	8.22	.35	1.43	.10	4.71	.27	4.85	.12	0.22	.05
1.68	7.50	.48	1.44	.15	4.95	.40	4.80	.17	0.07	.08
2.72	6.92	.51	1.39	.16	5.01	.44	4.65	.20	0.14	.09
3.71	6.34	.78	1.22	.24	4.24	.60	4.62	.27	0.29	.13
6.14	6.56	.54	1.33	.16	4.67	.45	4.31	.20	0.00	.10
7.46	6.30	.69	1.47	.20	4.22	.56	4.20	.25	0.12	.12
					NGC 4874 PA=65 r_e=51″					
0.42	...	...	1.49	.21	5.39	.58	5.22	.25	0.79	.12
1.23	8.33	.36	1.44	.11	4.95	.30	5.08	.13	0.07	.06
2.90	7.29	.42	1.39	.14	4.67	.36	4.80	.16	0.00	.08
4.94	7.04	.45	1.39	.16	4.73	.39	4.62	.17	0.24	.09
9.96	6.50	.46	1.43	.16	4.52	.39	4.43	.17	0.00	.09
					NGC 6166 PA=35 Major r_e=56″					
0.40	7.43	.64	-0.69	.25	0.96	.56	5.52	.37	2.56	.10
0.80	7.14	.46	-0.47	.15	1.89	.39	5.18	.24	2.08	.08
1.60	7.30	.47	0.49	.18	3.71	.41	4.76	.22	1.18	.08
2.40	6.95	.52	1.02	.19	4.86	.47	4.80	.23	0.58	.08
3.57	6.22	.40	1.35	.16	4.52	.37	4.44	.17	0.09	.07
5.17	6.28	.47	1.40	.19	5.09	.44	4.28	.21	0.00	.08
7.15	5.97	.45	1.44	.18	4.96	.40	3.88	.21	0.00	.08
10.26	5.41	.45	1.12	.18	4.31	.40	3.56	.21	0.00	.08
14.59	4.77	.53	0.35	.29	3.50	.42	3.35	.27	0.11	.10
					NGC 6166 PA=125 Minor r_e=41″					
1.60	7.13	.62	0.34	.25	2.72	.56	5.22	.31	1.73	.10
2.76	6.85	.49	0.96	.19	4.74	.46	4.92	.23	0.52	.09
4.71	6.44	.51	1.14	.21	4.97	.48	4.30	.23	0.01	.10
8.63	6.32	.60	1.43	.23	4.98	.56	4.27	.26	0.00	.11
11.29	6.05	.70	1.64	.27	5.16	.65	4.34	.32	0.11	.14
					NGC 7720 PA=190 r_e=42″					
0.33	...	...	0.40	.28	1.05	.39	5.32	.28	2.18	.14
0.66	...	...	0.85	.19	3.10	.41	5.23	.21	1.34	.10
1.32	...	...	1.42	.19	5.46	.45	4.99	.23	0.32	.12
2.26	...	...	1.84	.16	5.93	.42	4.90	.19	0.00	.11
4.35	...	...	1.53	.18	5.53	.45	4.44	.22	0.05	.12
5.43	...	...	1.61	.20	4.86	.48	4.35	.24	0.09	.14
					NGC 7720 PA=100 r_e=34″					
0.33	...	...	0.84	.25	2.70	.58	5.52	.30	1.66	.14
0.95	...	...	0.84	.14	3.62	.31	5.23	.16	1.00	.08
2.50	...	...	1.74	.16	5.52	.40	4.62	.17	0.00	.10
5.01	...	...	1.65	.20	4.86	.47	4.12	.21	0.11	.13
					NGC 7768 PA=60 Major r_e=33″					
0.33	...	...	1.39	.15	5.16	.32	4.73	.14	0.13	.08
1.60	...	...	1.31	.16	5.30	.37	4.53	.16	0.01	.09
3.79	...	...	1.42	.15	4.74	.36	4.24	.15	0.00	.10
7.89	...	...	1.18	.29	5.04	.65	3.93	.28	0.21	.19
					NGC 7768 PA=150 Minor r_e=25″					
0.33	...	...	1.36	.22	5.35	.49	5.01	.22	0.40	.12
0.66	...	...	1.35	.17	5.05	.38	4.69	.17	0.26	.10
1.59	...	...	1.38	.16	5.13	.36	4.34	.16	0.00	.10
4.49	...	...	1.34	.19	5.56	.39	4.03	.17	0.00	.11

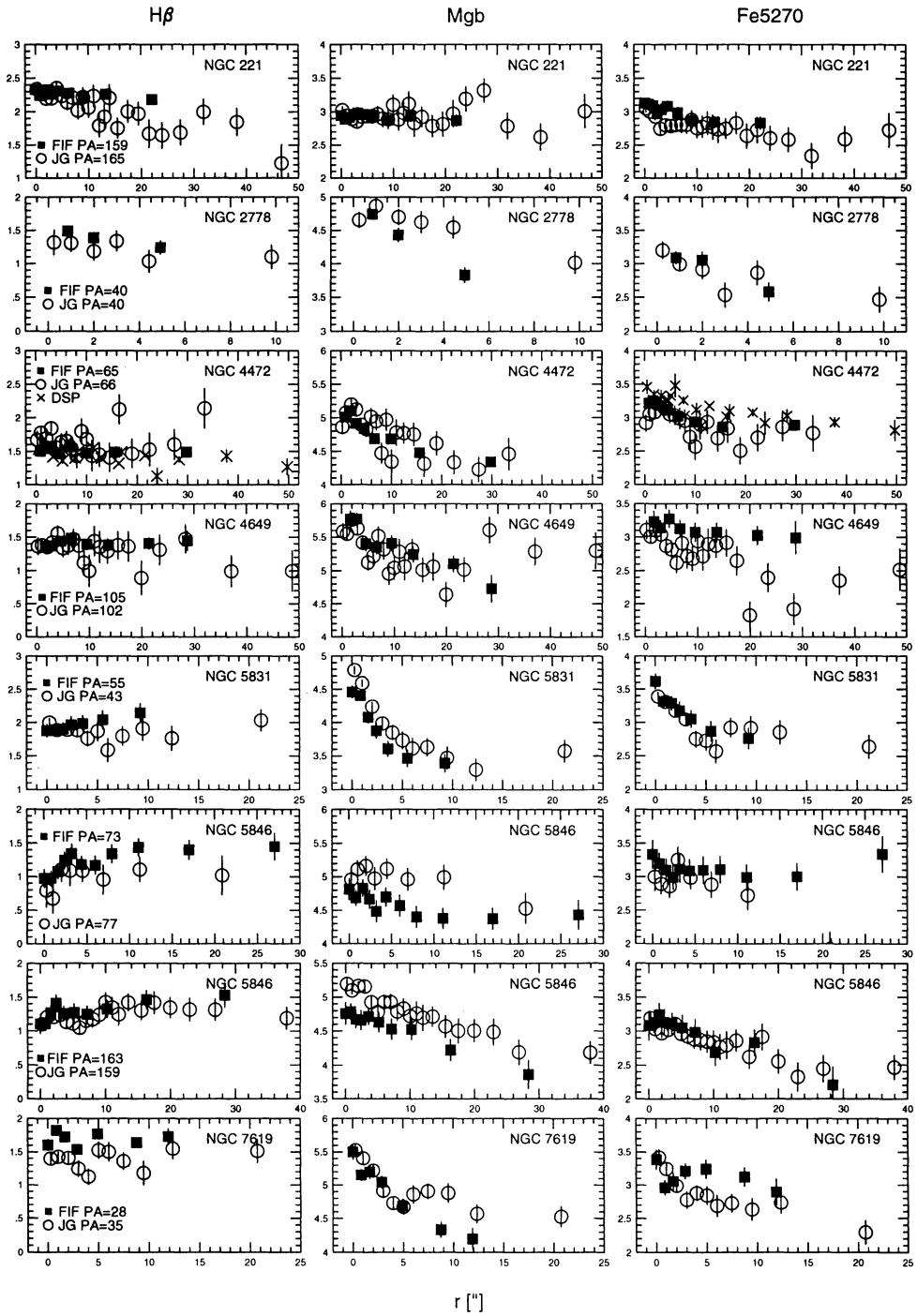

FIG. 9.—Comparisons between the Hβ, Mg *b*, and Fe5270 line strengths derived in the present study (*filled squares*), those from González (1993) (*open circles*), and for NGC 4472, from DSP (*crosses*). All line strengths are velocity dispersion corrected and calibrated to the Lick-IDS system. Indices are plotted against radius *r*, in arcseconds, along the indicated position angles.

The logarithms of the Mg *b*, Hβ, Fe4668, and Fe5015 line strengths are plotted in (*b*) as a function of r/r_e along the indicated position angles for the entire sample of observations. All line strengths are velocity dispersion corrected and calibrated to the Lick-IDS system. Least-squares fits to the profiles are shown as a solid line with the corresponding slope and its 1 σ error (in parenthesis). For objects with emission contamination, no fits were made to the Hβ and Fe5015 profiles, and in some cases the Hβ and Fe5015 values are plotted linearly.

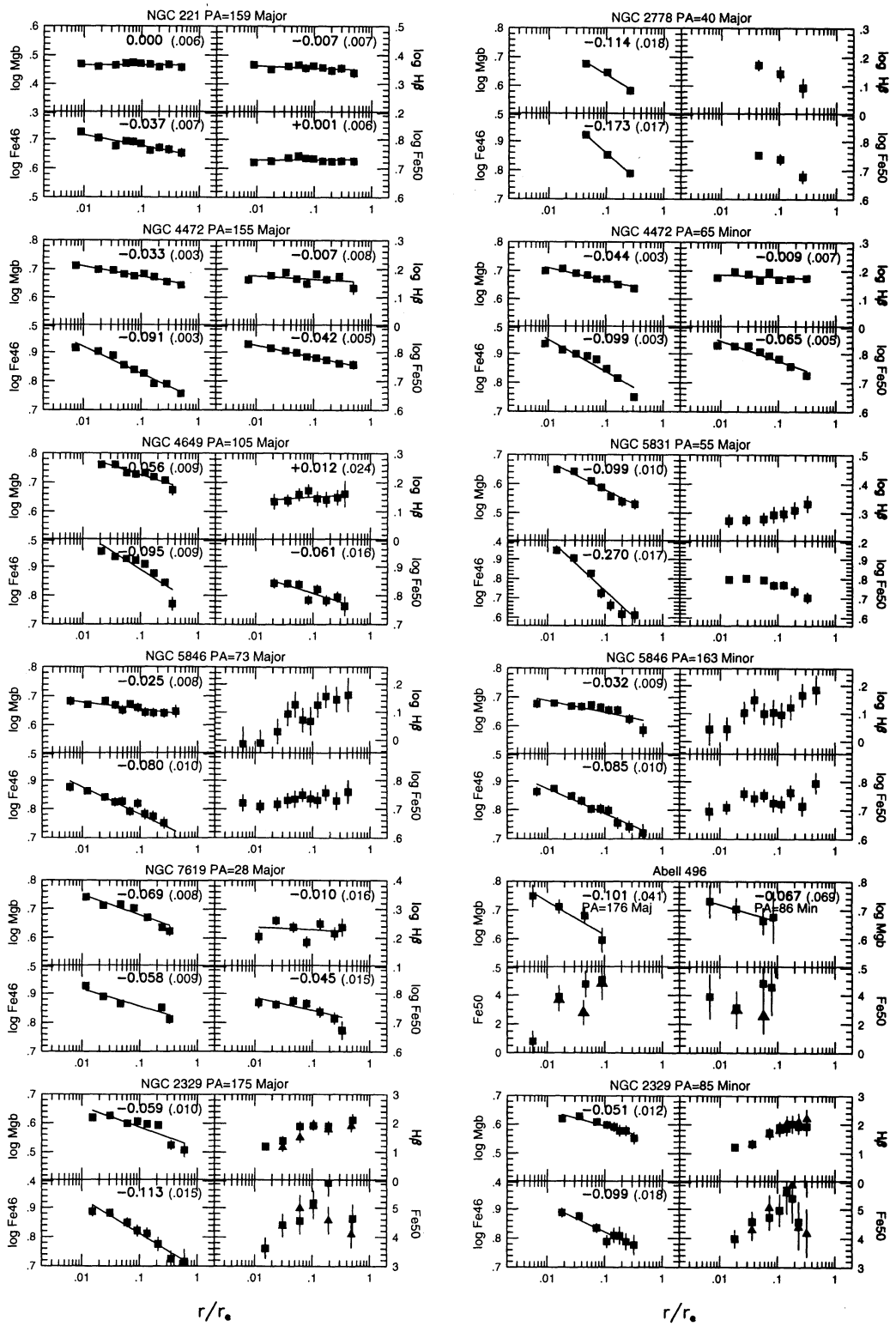

FIG. 9*b*

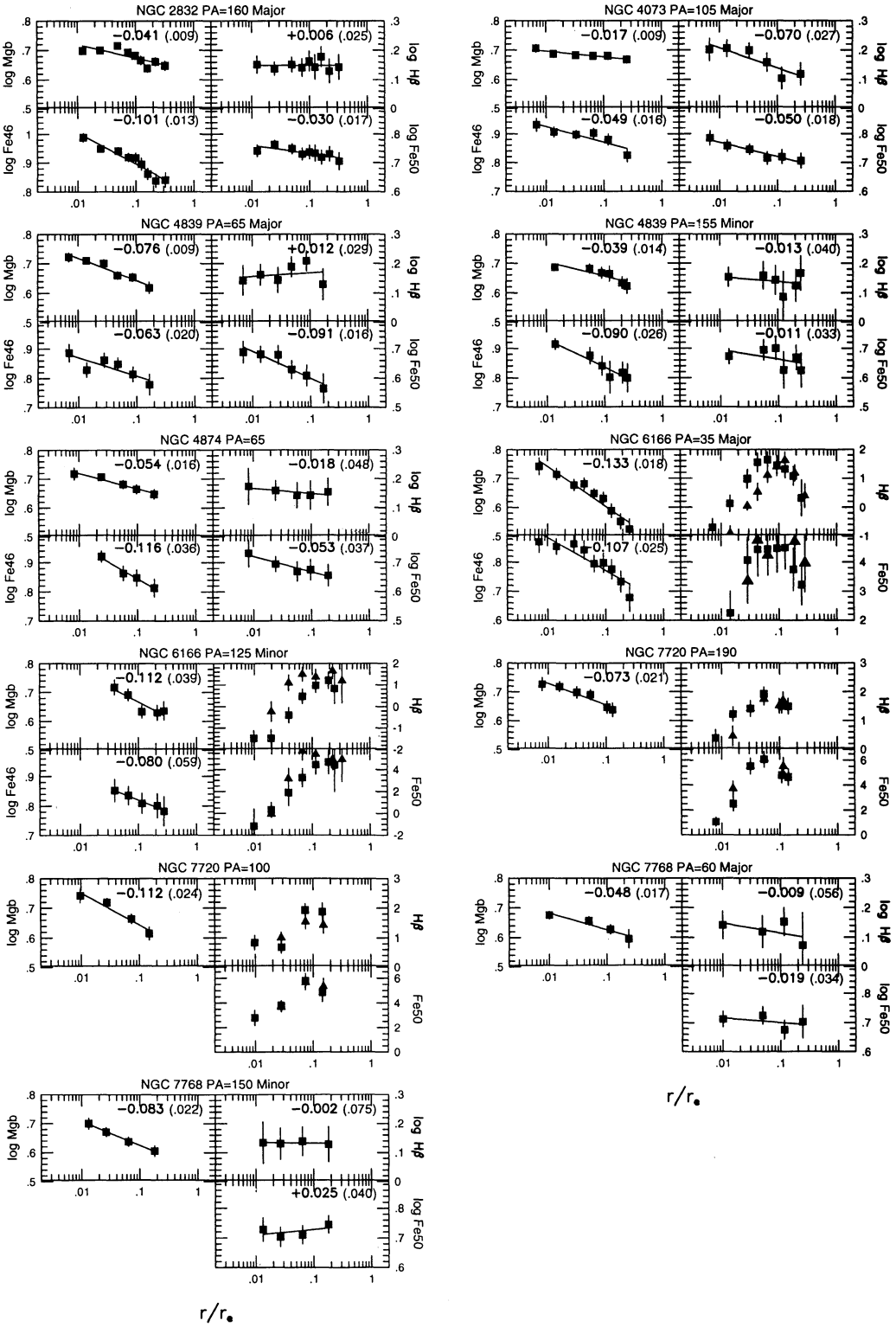

FIG. 9c